Contents lists available at ScienceDirect

Polymer Testing

journal homepage: http://www.elsevier.com/locate/polytest

Damage and failure in carbon fiber-reinforced epoxy filament-wound shape memory polymer composite tubes under compression loading

Zhaokun Ren [a], Liwu Liu [a,**], Yanju Liu [a], Jinsong Leng [b,*]

[a] Department of Astronautical Science and Mechanics, Harbin Institute of Technology (HIT), P.O.Box 301, No.92 West Dazhi Street, Harbin, 150001, People's Republic of China

[b] National Key Laboratory of Science and Technology on Advanced Composites in Special Environments, Harbin Institute of Technology (HIT), Harbin, 150080, People's Republic of China

ARTICLE INFO

Keywords:
Carbon fibers
Tube
Compression
Buckling

ABSTRACT

In this paper, axial and radial compression tests of carbon fiber/epoxy filament wound shape memory polymer (SMP) composite tubes were carried out to investigate the corresponding mechanical response. Carbon fibers impregnated with epoxy resin matrix were wound with $\pm 45^\circ$ layers. The effects of temperature, compression times, defect hole area, shape, and distribution on the mechanical properties of composite tubes were studied and analyzed, respectively. Meanwhile, the mechanical model of stress distribution about the defect hole, under axial compression loading, was established via using the method of complex function. Furthermore, the failure factors of specimens were analyzed. As a result, the defect with sharp angle would result in lower buckling load and Young's modulus. In addition, the failure area, where the delamination of materials, was predominantly located in the middle of specimen. The more times of compression to failure would result in the lower buckling load and Young's modulus of specimens, and the relationship was mainly in form of a specific power function. According to Hashin failure criteria, the effect of axial compression times on buckling load and equivalent modulus was investigated.

1. Introduction

CFRP (Carbon Fiber Reinforced Plastics), which the cylindrical structures have been widely used in industry communities, especially in pipeline systems, possess the excellent high specific strength and stiffness, high corrosion resistance and fatigue properties [1]. Composite tubes manufactured by filament winding method, possess more space for innovation in the fields of oil and gas [2]. Most filament-wound composite tubes are axial-symmetrical thin-walled structures, and the carbon fiber is wound around the symmetrical axis with an angle, of ($\pm\theta$) [3,4]. Compressive load testing with tubular specimens may result in global or local buckling instability [5]. Shape memory polymer composites (SMPCs) are intelligent materials with the ability to recover from temporary state to initial state under various external stimuli, such as heat, water, magnetic field or light. SMPCs have the ability to perceive the internal and external physical signals, taking corresponding actions to realize the controllable deformation of the structure [6–10]. Epoxy resin, while adopted with shape memory effect, could be employed as the matrix to fabricate composite tubes, which could exhibit the excellent deformability that traditional tubes do not have, and further expand the application fields. Composite tubes usually have some defects like holes, furthermore, the location, size, and shape of holes show different buckling characteristics. Meanwhile, owing to SMPC tubes possess the ability to recover to the initial state, the mechanical properties of tubes will be changed after compression buckling. The transverse compression stress of cylindrical shells will occur after buckling, because the instability of buckling form will lead to small initial defects. For cylindrical shells, buckling is equivalent to failure. There are many theoretical analysis methods for composite laminated structures. Zbigniew et al. revised the non-linear theory of orthotropic thin-walled plates, and applied perturbation theory to obtain the approximate solution of the equation based on Hamilton's principle. On the other hand, the transition matrix method was used to solve the problem of non-linear stability [11]. For simple composite sandwich plate-shell structures, Fan Jiarang et al. adopted space method to obtain exact solutions. Simultaneously, there were restrictive conditions for laminated plate and shell structure,

* Corresponding author.
** Corresponding author.
E-mail addresses: liuliwu_006@163.com (L. Liu), lengjs@hit.edu.cn (J. Leng).

https://doi.org/10.1016/j.polymertesting.2020.106387
Received 26 September 2019; Received in revised form 25 December 2019; Accepted 27 January 2020

i.e., rectangular plate, cylindrical shell or descriptive simple double curvature shell, especially in orthotropic laminated panel (overlapping angle of lamination and coordinate axis), boundary conditions that were simply supported, clamped or combination of both. On the premise of assuming the displacement form, Fan Jiarang et al. adopted Galerkin variational stress method in-plane to obtain the approximate solution of the deformation of simply supported plates [12,13]. Lin et al. adopted elastic foundation model to simulate the effect of sandwich on the surface panel, and applied virtual reaction between the surface panel with the sandwich core to replace the adhesion. As a result of the virtual reaction being zero at the layers, the analytical method could be used to solve the layered problem, and the layered buckling behavior of single and multiple layered sandwich plates with different shapes, sizes and locations was predicted [14]. Based on the elastic model, Cheng et al. studied the buckling modes of sandwich beams in local layers by Fourier series and Stockers transform method, obtaining the analytical method of residual strength on the sandwich plate with damage, under different end conditions [15]. Chai et al. proposed delaminated buckling and extended one-dimensional thin-film delamination and general delamination models [16]. Furthermore, Vizzini et al. have made a great improvement to the one-dimensional layered model and proposed a one-dimensional layered elastic foundation model, to show that Chai's model overestimates the buckling load of the layered structure [17]. P. M. Weaver et al. validated the buckling load of composite cylindrical shells with tension-torsion coupling effect under compression and studied the compressive properties of the structures with antisymmetric and symmetric layers [18]. Azam Tafreshi investigated the buckling and post-buckling behavior of composite cylindrical shells with rectangular holes under axial and internal pressures, and the results showed that the buckling load was inversely proportional to the size of the hole, yet directly proportional to the internal pressure. On the other hand, the buckling load was proportional to the height of the hole, under the condition of the same opening area [19]. Marco Cerini et al. studied the modal transformation of stiffened plates at the post-buckling stage by arc length method [20]. Ghannadpour found that the effect of small area holes on the buckling load could be neglected; nevertheless, the buckling load of the long axis of elliptical holes perpendicular to the loading axis was larger than that parallel to the loading axis [21]. Xu et al. introduced a Hamiltonian system to study the effect of local and global buckling behavior on the axial compression of cylindrical shells [22].

In this paper, we investigated the effects of the parameters on SMPC tubes, such as the opening at different positions, the area, and the shape of the hole, on the buckling instability of the cells. Owing to the unique shape recovery effect of SMPC, the specimens were heated and rebounded after compression, and the mechanical properties of the restored tubes were re-examined.

2. Experimental

2.1. Materials and manufacturing

The material system used was composed by Toray T800 carbon fiber and epoxy resin (E51) with shape memory effect. As shown in Fig. 1(a) and (b), the composite tube was manufactured by carbon fiber/epoxy resin wound with ±45°layers. The outer and the inner diameter of the tube was 126 mm and 120 mm, respectively, and the length was 3 m. Afterwards, the whole cell was processed into a great many of 100 mm high specimen tubes, as presented in Fig. 1(c), (d) and (e). After winding, the tube was heated and cured in the oven, cured at 80 °C for 3 h, 120 °C for 3 h, and 150 °C for 5 h. Then, the system was cooled to room temperature, and the tube was removed from the mandrel. Meanwhile, some holes of different sizes and shapes were opened on the wall of some specimen tubes to achieve the purpose of creating defects. As shown in Fig. 2, two circular cutouts with a diameter of 50 mm and 80 mm, four elliptical cutouts (long axis: 60 mm; short axis: 40 mm), respectively, and two rectangular cutouts with 50 mm and 80 mm were manufactured on the wall of some tube specimens. In Fig. 3, the buckling behavior of different specimen tubes was further considered on the premise of the equivalent defect area.

2.2. Characterization

The compression test was measured at strain rate of 0.02/min. The specimen was placed between two metal plates of the compressor. Simultaneously, the upper plate was compressed downward, and the lower plate was fixed. Axial compression failure position was likely to

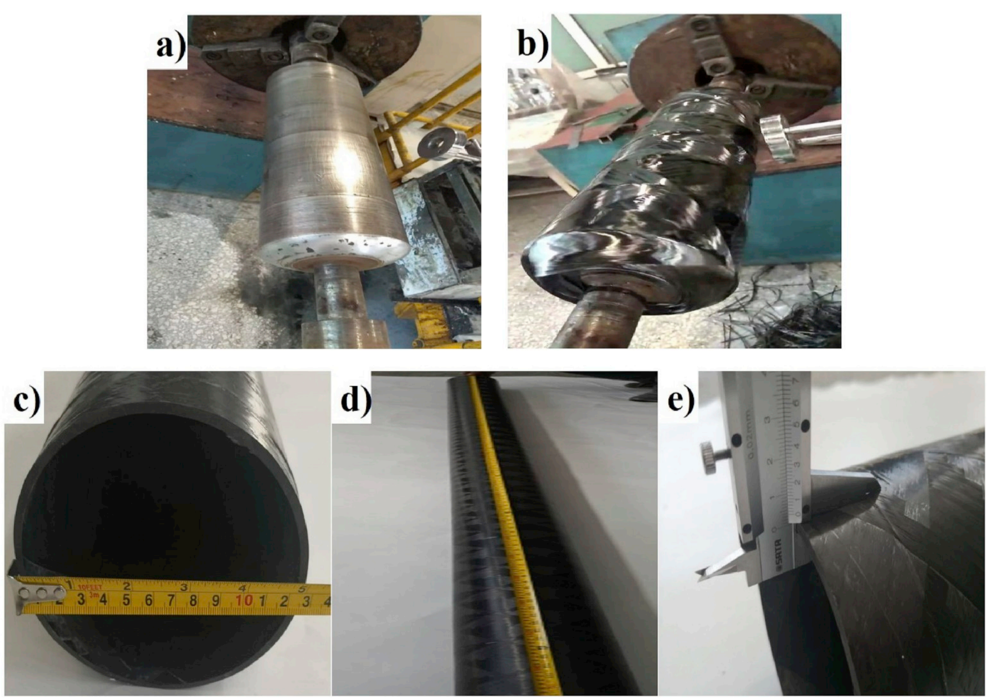

Fig. 1. The winding mold (a) and process (b) of composite tube, respectively. Dimensional diagram of composite tube (c)(d)(e).

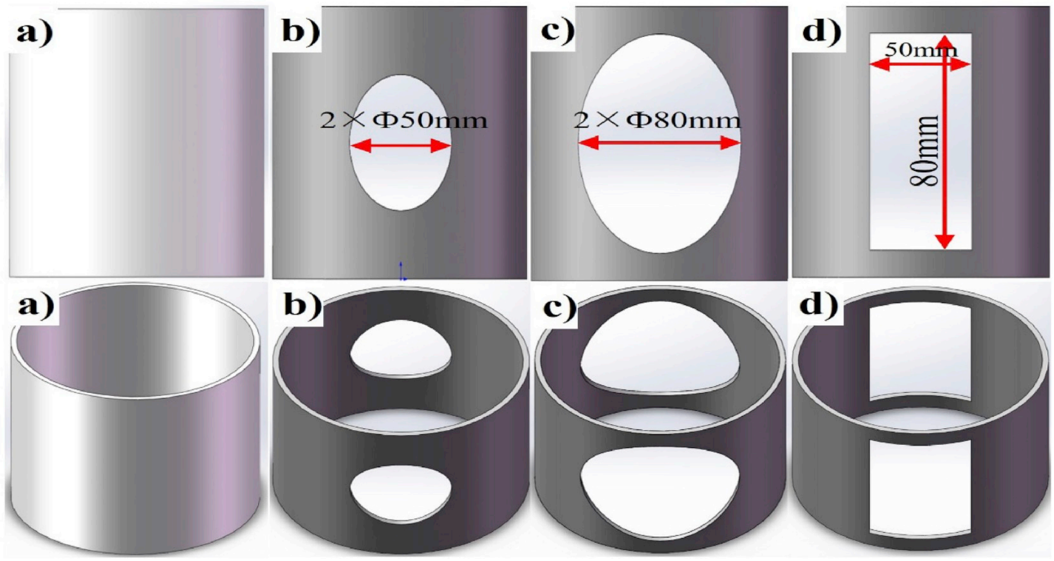

Fig. 2. Specimens with different opening area and shape: (a) Without cutout. (b) Circular cutout (2 × φ50mm). (c) Circular cutout (2 × φ80mm). (d) Rectangular cutout (2 × 50*mm* × 80*mm*).

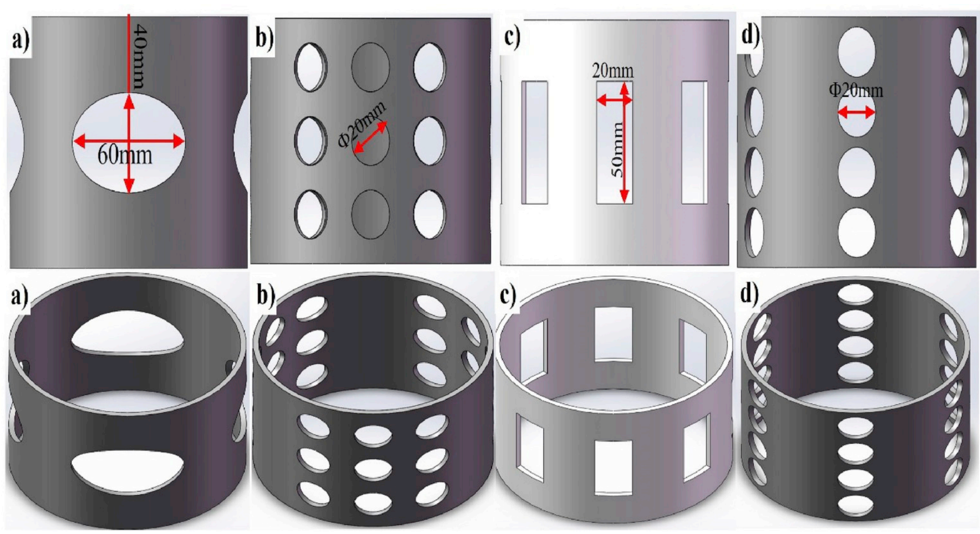

Fig. 3. Specimens with identical opening area but diverse shapes of openings: (a) Elliptical cutout (4 × 60*mm* × 40*mm*, long axis: 60 mm; short axis: 40 mm) (b) Circular cutout (27 × φ20mm) (c) Rectangular cutout (8 × 20*mm* × 50*mm*) (d) Circular cutout (24 × φ20mm).

occur in the middle or end of the specimen. It was difficult to calculate the fiber content in the specimen prepared by the winding method. Therefore, thermogravimetric analysis (TGA) method is required to determine the fiber content. The glass transition temperatures (Tg) of epoxy resin with shape memory effect are 120 °C and 150 °C, respectively. Nevertheless, owing to the high fiber content of composite tubes made by winding, DSC (differential scanning calorimetry) method is required to confirm the glass transition temperatures. Meanwhile, the material structure before and after the compressive testing was observed by SEM (Electron Scanning Electron Microscope) and optical microscope. In addition, the surface roughness of specimen before and after the compressive testing was followed by stereomicroscope (refer to section S1, S2, S3, S4).

3. Results and discussion

3.1. Morphology of SMP composites

In this paper, carbon fiber/epoxy resin was used for winding 20 layers to prepare specimens. As shown in Fig. 4(a), carbon fibers were tightly coated with the epoxy resin matrix. The winding direction of carbon fibers was distinct, simultaneously, the layers of carbon fibers were stratified, and the thickness of each segment on carbon fibers were about 0.15 mm, as present in Fig. 4(b).

Fig. 5 is a scanning electron microscopy (SEM) images of the laminated position of the composite tube after compression testing. After delamination, the fibers and epoxy matrix have been entirely debonded. In most cases, the fibers were pulled out from the matrix. As shown in

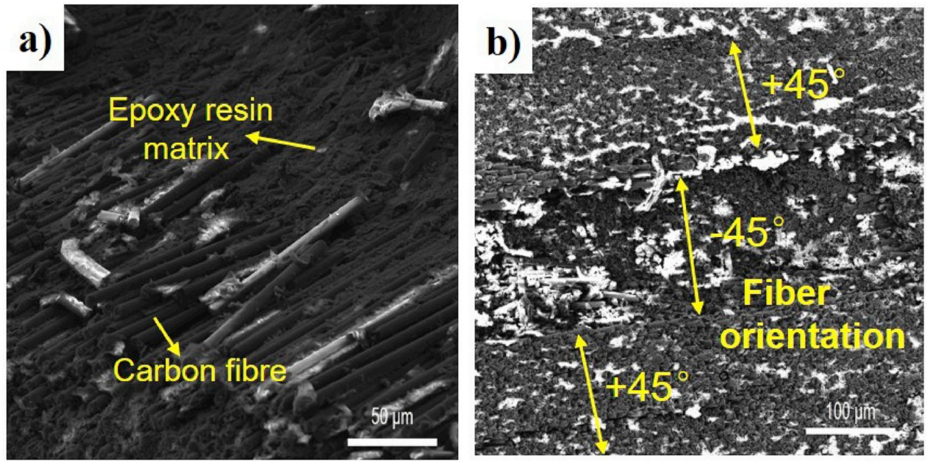

Fig. 4. Section Electron Microscope of shape memory polymer composite specimen tubes before compressive testing.

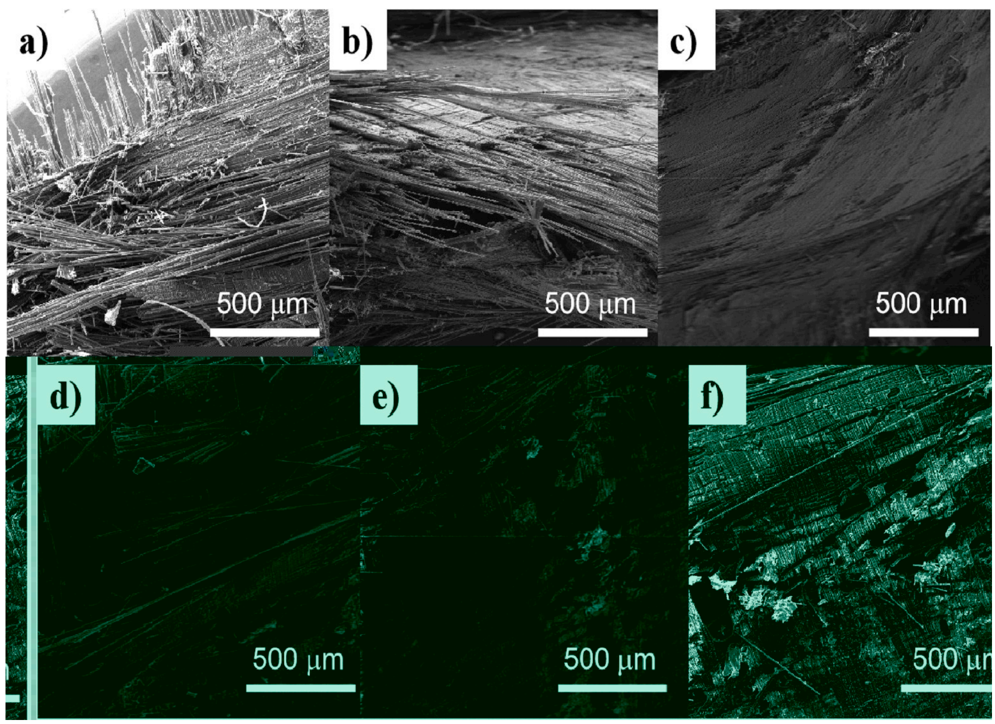

Fig. 5. Section Electron Microscope of shape memory polymer composite specimen tubes after compressive testing.

Fig. 5, after compression testing, the failure mode of composite tubes could be attributed to the debonding between the matrix with the fibers; additionally, the fibers were pulled out from the matrix. Section S1 and S2 can be used to observe the image of the sample before and after compression by stereomicroscope and optical microscope. Section S3 and S4 can be used to determine the fiber content and glass transition temperature range of the composite tube.

3.2. Compressive testing and analysis

SMPC have the effect of restoring the original shape after being stimulated by external forces, as shown in Fig. 6. Therefore, the relationship between the number of spring back with yield load, equivalent modulus, and stiffness can be further studied. The compression test was measured at strain rate of 0.02/min, simultaneously, the main research was the change about mechanical properties of SMPC tubes after compressive failure, reheat rebound, multiple compression, and heating rebound. Stiffness (S), stress (σ), equivalent modulus (E_{eq}), strain (ε) are calculated as follows:

$$S = F/D \tag{1}$$

$$\sigma = F/A \tag{2}$$

$$\varepsilon = D/l \tag{3}$$

$$E_{eq} = \sigma/\varepsilon \tag{4}$$

Where F is the applied load, D is the displacement and deflection, A is the cross-sectional area, l is the specimen length.

3.2.1. Radial compression

The diameter of the tube decreases in the vertical direction and enlarges in the horizontal direction, forming an elliptical shape. As shown in Fig. 7(a), the variation trend on load-deflection curves with different

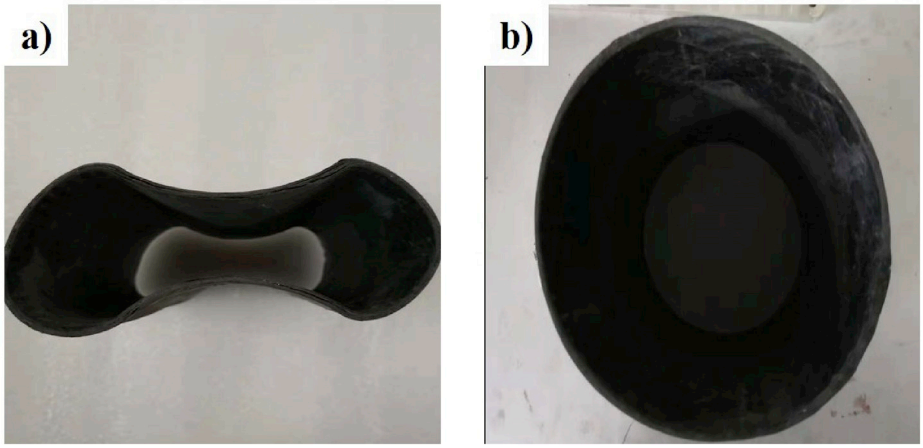

Fig. 6. Specimen tube after compressive deformation (a) and specimen tube spring back after external excitation (b).

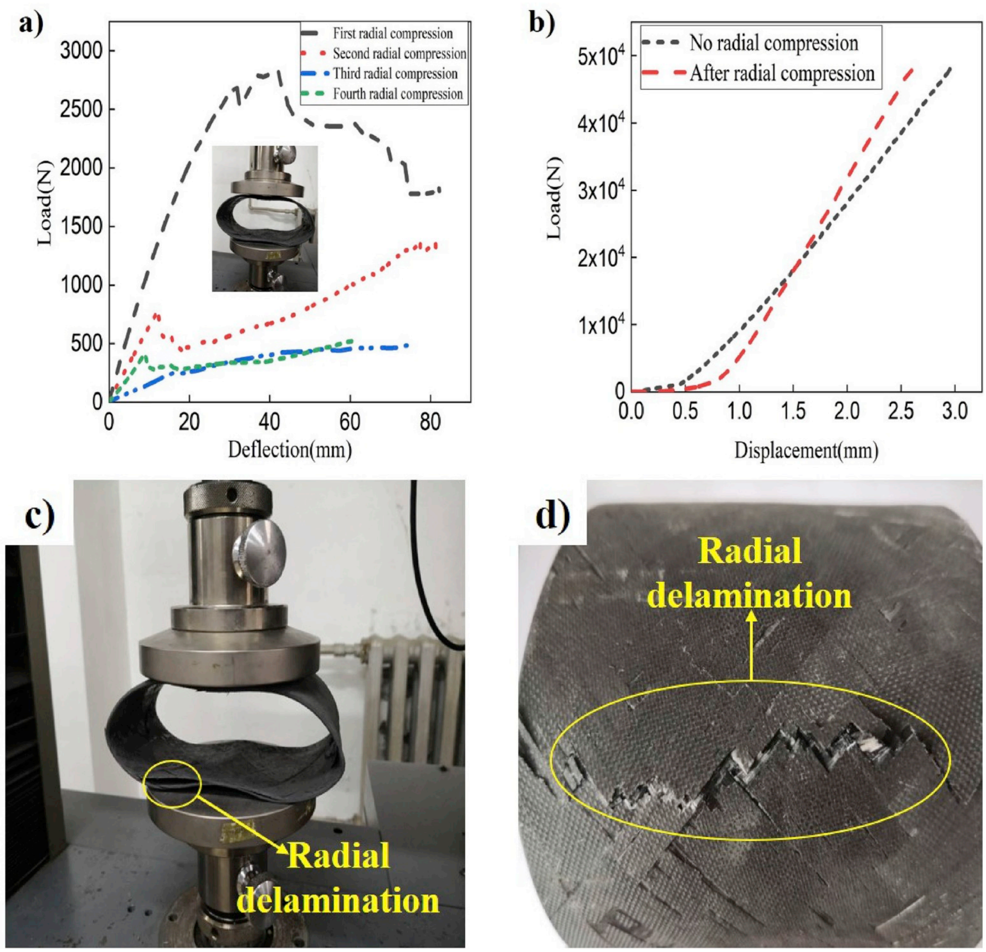

Fig. 7. (a) Deflection-load curves under different radial compressive numbers. (b) Axial compression of specimen tube without radial compression and after four radial compression: load-displacement curves. (c)(d) Layer diagrams of specimen tube after radial compression failure.

radial compressive times could be seen from the figure, where the yield load and deflection were huge during the first radial compression. The yield load and deflection of the specimen tube, which was stimulated to rebound, decreased obviously after the second radial compression. As the third radial compression occurs, the yield load and deflection decreased again. After the fourth radial compression, there was no visible yield phenomenon, which indicated that the specimen tube had completely failed but not rebound. The failure modes of radial compression were mainly transverse cracking and delamination, yet the fibers break less, i.e., the radial compression submitted to the external energy of resin, not fibers. The external loading leaded to the failure behavior of epoxy resin between the composite layers to cause the transverse delamination phenomenon. In the linear portion of the load-deflection curve, the specimen exhibited elastic behavior without showing failure phenomenon. After reaching the non-linear peak value, the specimens revealed a trend of delamination and failure behavior.

Owing to the shape memory effect of epoxy resin, the resistance would occur after external excitation. The resilience can be restored to the original state, but not recover the fiber and resin matrix to the original bonding state. The viewpoint is corroborated by the stratification phenomena in Fig. 7(c) and (d). The mechanical response of the specimen tube without radial compression and the specimen tube after four radial compression is shown in Fig. 7(b). As present in Fig. 7(b), the load-displacement curves of the two methods were remarkably similar, so the radial compression failure had little effect on the axial stiffness of the structure, which validated that the interlaminar shear stress exceeded the allowable interlaminar mechanical strength, leading to the radial delamination in the radial compressive testing. Furthermore, the axial mechanical properties of specimen structure did not show the significant impact. It was proved that the fibers had no fracture, yet the resin between the radial bonding layers failed. The corresponding mechanical model can refer to section S5 and S7.

3.2.2. *Axial compression*

The composite tube with shape memory effect on the axial mechanical properties of the structure can be investigated by the axial compressive testing. There were many investigations on the effect of defect holes on the buckling behavior of traditional materials, yet few on the effect of shape memory effect on the buckling behavior of shape memory polymer materials. On the other hand, it could be diverse for the mechanical response of the composite tube under axial compressive testing at different temperatures.

A 200 mm long composite tube (126 mm in outer diameter, 120 mm in inner diameter, laminate $[\pm 45^{\circ}]_{20}$) was used for an axial compressive testing, as shown in Fig. 8. As the axial compressive displacement was 2.96 mm, the compression load reached ca. 47.4 kN, therefore, the equivalent modulus of the specimen was determined to be 2.75 GPa. In addition, the load simulated by ABAQUS was ca. 48.3 kN, simultaneously, the difference between the simulation and the test was ca. 1.9%. As a result, the accuracy of the simulation analysis can be determined. As present in Fig. 8, the experimental curve has lower axial stiffness in the initial stage, and the stiffness increased after the displacement reached ca. 0.5 mm. In the same displacement range, the simulation curve was always above the experimental curve, which showed the energy output by the external load during the simulation process was higher than that of the experimental procedure, owing to the fact that the energy output induced by the external load during the simulation process was higher than that of the experimental procedure. The data of the equivalent modulus obtained in the test process had a certain degree of dispersion, simultaneously, in the process of selecting

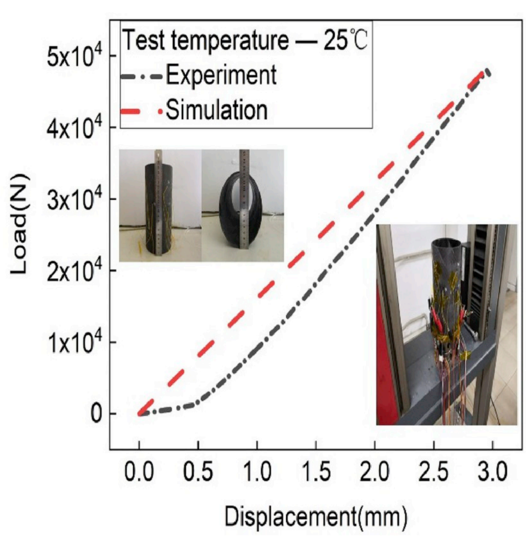

Fig. 8. Axial compressive load-displacement curves at room temperature.

the equivalent modulus as the simulation parameter for simulation, there will be a certain error with the test. On the other hand, this error was mainly due to the larger equivalent modulus parameter used in the simulation, so the output energy of the simulation process was higher. In the initial axial compressive process, the fibers of composite tubes were bonded by epoxy resin. During the compressive process, the fiber layers bonded via epoxy resin were continuously extruded, which increased the compactness of the structure and leaded to the improvement on the axial stiffness of the specimen tubes. In the simulation process, the phenomenon that the axial stiffness will increase, as the axial displacement reached a critical value, was neglected, in the meantime, the fitting data measured by experiments were directly used as parameters, which resulted in higher energy generated by simulation.

Epoxy resin is a kind of polymer; consequently, Young's modulus of CFRP composites will change obviously with the variation of temperature, which can also be seen from Fig. 9(d), that is, the axial equivalent modulus decreases with the increase of temperature. As present in Fig. 9 (a), the load-displacement curves of composite tubes were basically identical at 50 °C and 80 °C, nevertheless, at 120 °C the curves tended to be non-linear after a linear variation, indicating that the composite tubes tended to buckle. Local buckling phenomenon occurred when the experimental temperature was 150 °C, and the external load reaches 20.93 MPa, simultaneously, the buckling position was in the middle of the specimen tube. In addition, many studies have come to the conclusion that the local buckling position is in the middle of the specimen tube. With regard for comparing the simulation with the experimental results, as shown in Fig. 9(c), it could be concluded that the simulation data was basically higher than the experimental data, which could be consistent with the conclusion as shown in Fig. 8. After buckling, the composite tube with shape memory effect rebounded after external heating and compresses axially again, as present in Fig. 9(b), as the axial displacement reached 20 mm, the external load was much lower than that without buckling, which showed that SMPC tube recovers to the original state after external excitation, yet the structure strength not. Axial compression was mainly caused by the load acting on the matrix rather than carbon fibers. Besides, the matrix material was delaminated and debonded with carbon fibers, resulting in failing.

The existence of defects will affect the stiffness, strength, and buckling properties of composite tube structures; simultaneously, the influence is determined by the location and size of defects. In addition, the resin matrix used in this paper has shape memory effect; therefore, the shape rebound of the specimen tube which has buckled under axial compression loading can be achieved by external excitation, and the corresponding mechanical properties will also change, furthermore, the influence of the defects is required to study. Fig. 10 shows two holes with a diameter of 50 mm are machined in the symmetrical part of the middle of the specimen tube as the defects introduced.

As present in Fig. 10(a), in reference to the axial compression curve of the specimen tube, it could be found that the buckling behavior of the specimen tube does not occur at 50 °C, yet occurred at 120 °C when the external load reached 30.58 MPa, nevertheless, the buckling behavior of the defect-free tube did not occur at 120 °C (seen in Fig. 9(a)), which showed that the existence of defects did have an impact. Meanwhile, it is found that the place, where local buckling occurred, was also the middle part of the specimen tube, and the same was the transverse delamination, but more evident in the defect area. On account of the introduction of defects increasing the free boundary of the specimen, the high interlaminar shear stress at the free boundary resulted in the debonding phenomenon in the relevant area. On the other hand, as shown in Fig. 10 (a), the shape of the specimen tube recovered thoroughly after the external excitation rebound, but the axial stiffness decreased dramatically when the specimen tube was subjected to axial compression again, simultaneously, as local buckling behavior occurred again, the buckling load decreased, nevertheless, as the axial displacement reached a critical value, the load also showed an upward trend which could be seen from the axial compressive images that the defect has been wholly deformed

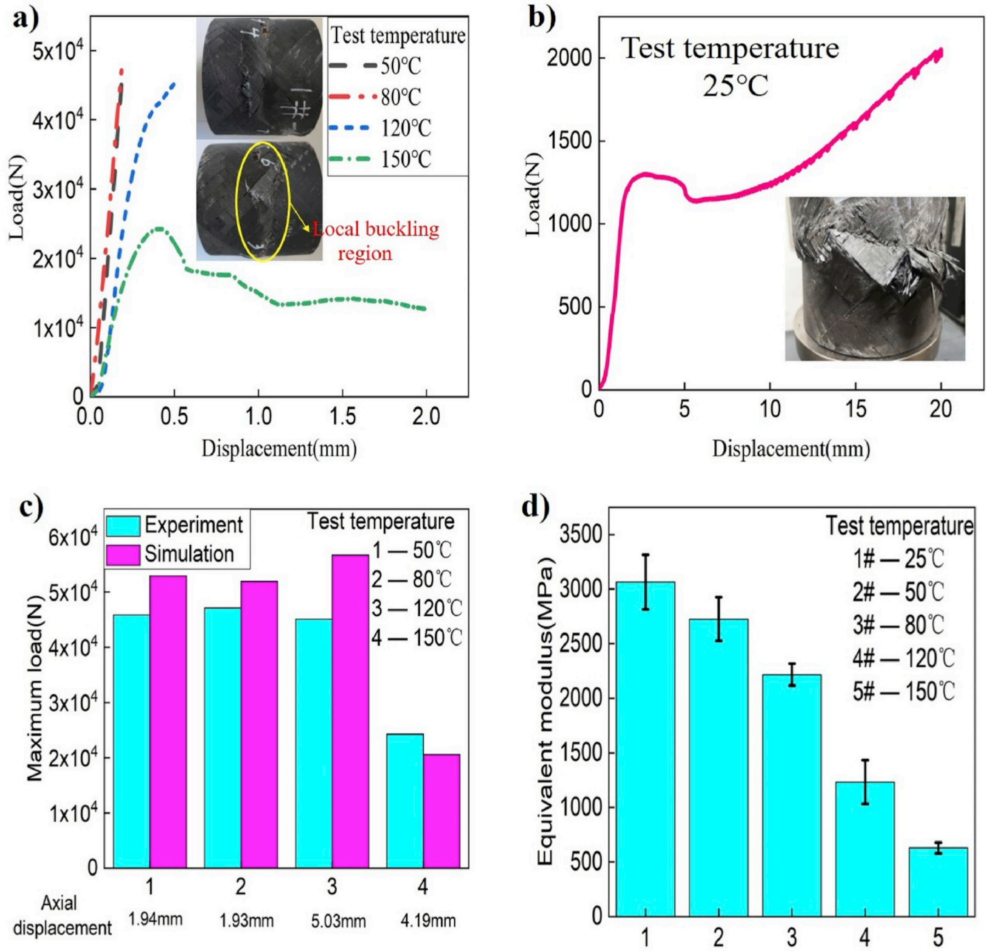

Fig. 9. (a) Axial compression displacement-load curves at different test temperature (50 °C, 80 °C, 120 °C, 150 °C). (b) Load-displacement curves of specimen tube under rebound and re-axial compression (25 °C). (c) Axial displacement under maximum external loading at different temperature (experiment and simulation). (d) Axial equivalent modulus of specimen tube at different temperature.

at this time, as a result of the axial displacement being hindered by carbon fibers, forming a new supporting structure, and the external load began to rise. However, the specimen tube that was subjected to external excitation, was incapable of rebounding again, which indicated that the resilience of the matrix was unable to overcome the deformation of the structure. Thus, not all the deformed structures could recover to the original state. Comparing the data of experiment and simulation, the difference between experiment and simulation could be neglected, as shown in Fig. 10(b); consequently, the stress distribution obtained by simulation was credible. Fig. 10(c) and (d) are the stress distribution contours of the specimen tube at 50 °C and 120 °C, respectively, as the maximum external load is achieved. The location of the maximum Mise stress was the middle part of the circular hole defect, which was consistent with the experimental results, that was, the region where the local buckling deformation occurred first.

Fig. 11 shows two holes with a diameter of 80 mm machined in the symmetrical position of the middle of the specimen tube as the defects introduced. In comparison to Fig. 10, the size of the defect hole was larger, yet the relative position of the defect hole was unchanged, which was used to observe the mechanical response of the specimen tube under axial compression loading as the size of the defect changing. As present in Fig. 11(a), the buckling of the specimen tube was still not observed at 50 °C, but local buckling occurred at 120 °C as the external load reached 20.54 MPa. Nevertheless, the buckling load was lower than 30.58 MPa in Fig. 10, which indicated that the increase of defect size reduced the buckling load. With the rebound of the specimen tube subjected to external excitation, the load-displacement curve of the specimen tube was approximately the same as that of the curve in Fig. 10(a), as compressed axially again. In Fig. 11(b), the experimental and simulated results were compared, in addition, under the condition of the same axial displacement, the experimental load was much higher than that of the simulated results, in the meantime, Fig. 11(c) and (d) show the same conclusions as Fig. 10(c) and (d).

Two symmetrical rectangular holes (50 mm × 80 mm) were machined in the middle of the specimen tube as defects. In comparison to Figs. 10 and 11, the shape of the defect was changed to analyze the effect of different defect shapes on the mechanical response, under the condition of axial compression loading. As present in Fig. 12(a), the buckling behavior of the specimen tube was still not observed at 50 °C, but local buckling occurred at 120 °C as the external load reached 27.6 MPa, where the buckling load was between that of the defect holes (that is, 50 mm in diameter and 80 mm in diameter, respectively). The local buckling load was 18.85 MPa when the composite tube was rebounded by heating and then compressed axially. The region where local buckling occurred, was roughly in the middle of the specimen tube, simultaneously, the deformation occurred at the sharp corner of the rectangular defect. In Fig. 12(b), it is found that the experimental and simulation results are compared, and the conclusions are roughly the same as those in Fig. 11(b), both of which are higher than the simulation values. Fig. 12(c) and (d) are the stress distribution contours of the maximum load at the experimental temperature (that is, 50 °C and 120 °C, respectively). As seen in Fig. 12(c) and (d), the maximum stress is

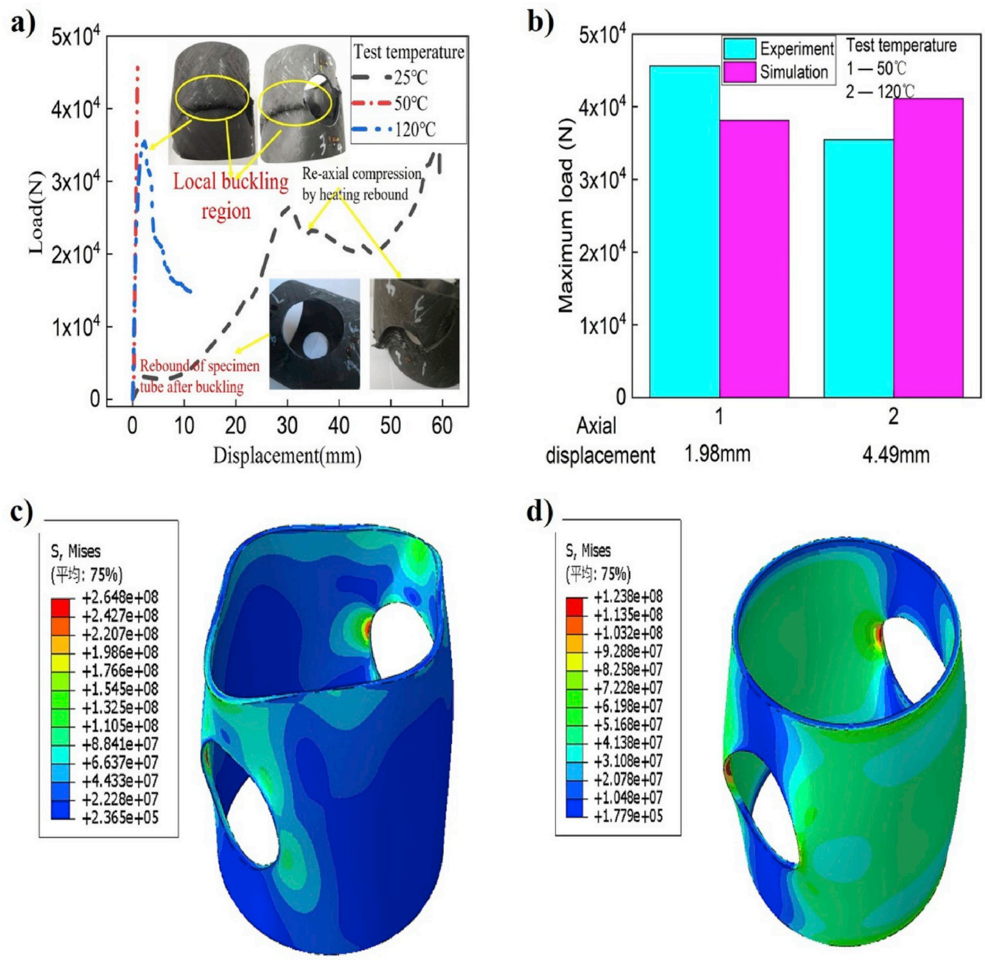

Fig. 10. Two holes of 50 mm diameter are machined in the relative symmetrical position in the middle of the specimen tube: (a) The load-displacement curves of the specimen tube under axial compression loading at 50 °C and 120 °C, respectively, and at 25 °C after rebound are obtained. (b) Contrast diagram of maximum load achieved at the same displacement (experiment and simulation). (c) Stress distribution under maximum external loading at experimental temperature (50 °C). (d) Stress distribution under maximum external loading at experimental temperature (120 °C).

concentrated in the middle of the specimen tube and the sharp corner of the rectangular hole, which is consistent with the experimental results.

The temperature and defect area, as well as the shape of the defect, was investigated in the above-mentioned specimen tubes. Nevertheless, under the condition of the same total defect area, the influence of the defect shape and distribution on the local buckling of the specimen tubes was required to be further studied (refer to section S6).

Fig. 13 shows that four elliptical holes (long axis: 60 mm and short axis: 40 mm) are uniformly distributed in the middle of the specimen tube as defects. Fig. 13(a) is the load-displacement curve of the specimen tube under axial compression loading, where the first axial compression buckling occurs. Simultaneously, the buckling position is in the middle of the specimen tube, and the fiber delamination phenomenon occurs, yet few fibers break. After rebounding after heating, the second, third, and fourth axial compression showed that the specimen tube had basically lost the keeping resisting. In Fig. 13(b), the experimental and simulated curve of the first axial compression, where the trend was approximately the same, nevertheless, the simulated buckling load was 11.56 MPa, which was much smaller than the experimental buckling load (29.27 MPa), showing that the strength of the actual specimen was much higher than that of the simulation data on the premise of the axial equivalent modulus being 1.53 GPa. In Fig. 13(c), the stress distribution of the specimen tube under buckling load was analyzed, and the stress concentration occurred at the end of the long axis of the elliptical defect hole, which was consistent with the actual situation. In the process of axial compression, the failure and the delamination, which extended to the whole central region, firstly occurred at the end of the long axis.

As present in Fig. 14, six rows were evenly distributed, and each row had four defective holes with a diameter of 20 mm, simultaneously, the distance between the two adjacent holes in each row was 24 mm, referencing to Fig. 3(d). Compared with Fig. 13, the total area of defect holes in the specimen tube in Fig. 14 is the same, but the distribution is not. No local buckling behavior occurred during the axial compressive testing of the specimen tube in Fig. 14(a). After four times of axial compression, the load-displacement curves obtained by each compression of the specimen tube were approximately the same, indicating that the strength of the structure was without decreasing with the increase of the number of external loading. In Fig. 13, the buckling behavior of the specimen tube with elliptical defect holes occurs, which indicated that the defect area was the same, nevertheless, the yield load of the whole structure increased when the defect area was uniformly distributed, and the average area of each defect was smaller than that of the structure with concentrated defects. Fig. 14(b) is the stress distribution diagram of the specimen tube under the maximum axial compression load, and the location where the maximum stress occurs is also the transverse end of the circular hole. It was noteworthy that the maximum stress in Fig. 14 (b) was far less than that in Fig. 13(c), which indicated that dispersing the defects is beneficial to enhance strength.

Although the strength of the specimen tube with dispersed defects was higher than that of the specimen tube with concentrated defects, the diameter of dispersed defect holes remained unchanged and the number of defects increased, leading to structural strength reduction. As present in Fig. 15, the number of defect holes with a diameter of 20 mm was increased up to 27, and the distribution of holes can be referred to Fig. 3 (b). As seen from Fig. 15(a), as the experimental load reached ca. 39.84 MPa, local buckling occurred, simultaneously, the simulated yield load was 18.54 MPa. Nevertheless, the post-buckling trend of the experiment and simulation was almost the same. In addition, the failure location of

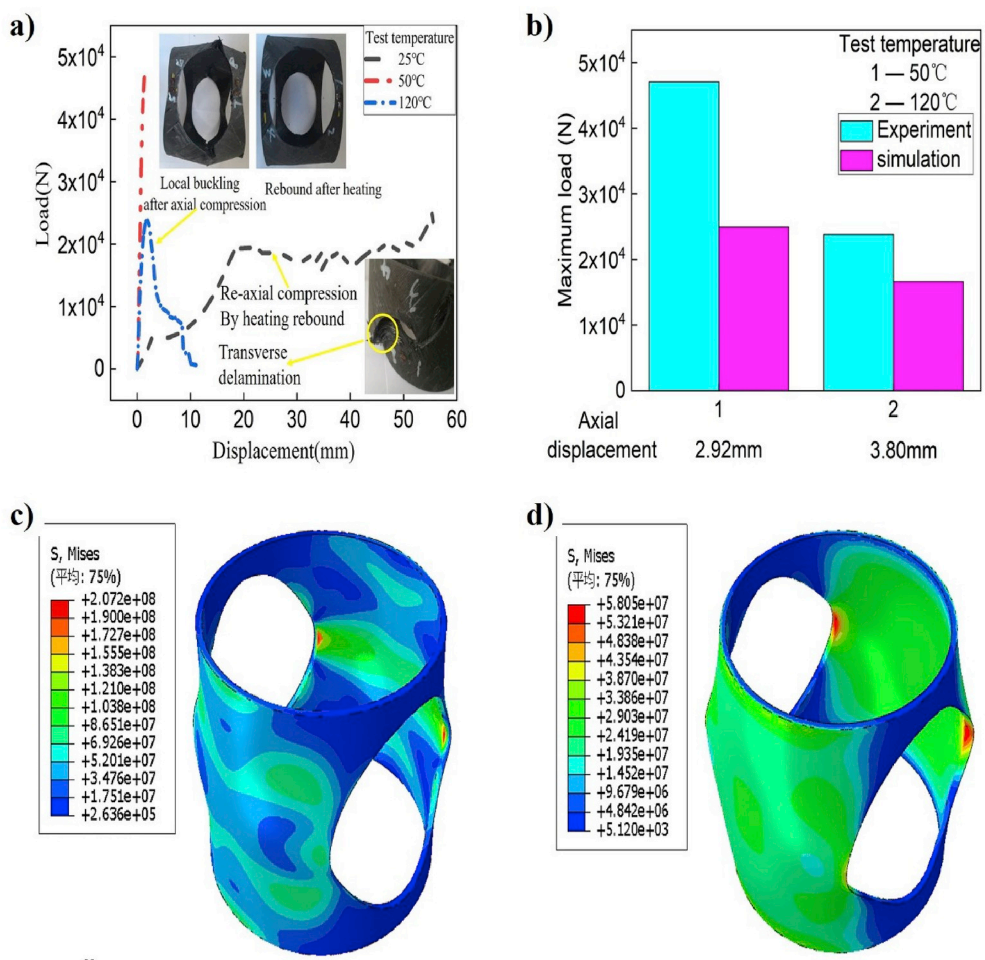

Fig. 11. Two holes of 80 mm diameter are machined in the relative symmetrical position in the middle of the specimen tube: (a) The load-displacement curves of the specimen tube under axial compression at 50 °C and 120 °C, respectively, and at 25 °C after rebound are obtained. (b) Contrast diagram of maximum load achieved at the same displacement (experiment and simulation). (c) Stress distribution under maximum external loading at experimental temperature (50 °C). (d) Stress distribution under maximum external loading at experimental temperature (120 °C).

the specimen tube was primarily at the top and bottom of the defect hole array, and the failure mode was mainly the transverse delamination of fiber/matrix. In other words, as the axial load reached the strength of the matrix, the increase of interlaminar shear stress at the failure location resulted in the delamination. Concurrently, in the process of axial compression, the fibers were continuously pulled out from the matrix with the increase of the axial displacement after delamination. As present in the stress contour of Fig. 15(b), the maximum stress occurred mainly on both sides of the upper and lower holes of the defect hole array, which was in agreement with the experimental results.

Owing to the shape memory effect of the resin matrix, the yield load, stiffness and equivalent modulus of the specimen tube would change significantly after axial compression and rebound under external excitation. To determine the relationship between compression times with stiffness and equivalent modulus of SMPC tube, the thickness of specimen tube was designed as 1 mm, the outer diameter was 107 mm, and the height was 100 mm. Furthermore, the thin-walled structure ensured that the test tube could be compressed to failure buckling under the condition of allowable range of the press.

Fig. 16 shows the mechanical response of the specimen tube under different axial compression times at room temperature. In Fig. 16(a), the load-displacement curves of the specimen tube which possessed shape memory effect of rebound after external excitation, were shown under different axial compression times. As present in Fig. 16(a), with the increase of the number of axial compressions, the load-displacement curve has also undergone obvious changes. As the buckling load decreased continuously, and the slope of the curve in the linear part, i.e., the stiffness decreased, and the displacement in the linear region decreased. In addition, the location of local buckling was in the middle of the specimen tube, which was consistent with the previous axial compressive testing. In Fig. 16(b) and (c), the stiffness and yield strength of the specimen tube under different axial compression times were sorted out. With the increase of compression times, the related mechanical parameter decreased obviously, indicating that the specimen tube of the corresponding mechanical properties was irrecoverable after external excitation and rebounds. Fig. 9(c) and (d), Fig. 16(b) and (c) are fitted power functions of equivalent modulus, yield strength and axial compression times, experimental temperature, respectively, and the fitting functions are expressed as follows:

$$E_{eq} = 2.699n^{-1.257}\text{GPa} \tag{5-1}$$

$$E_{eq} = \left(-0.00273t^{1.378} + 3.312\right)\text{GPa} \tag{5-2}$$

$$\sigma_s = 28.28n^{-1.205}\text{MPa} \tag{6-1}$$

$$\sigma_s = \left(376.6t^{-0.05871} - 253.5\right)\text{MPa} \tag{6-2}$$

E_{eq}— Equivalent modulus; σ_s— Yield strength;
n—Axial compression times; t—Temperature (°C)

Equivalent modulus and yield strength should be functions of compression times and temperature, as shown in equations (5) and (6).

The failure modes of axial compression are mainly determined by matrix failure, which could be related with transverse load (σ_2) and shear load (τ_{12}), indicating that the matrix has failed as the load-displacement curve of the specimen changes nonlinearly [23,24]. When the stress-strain curve of the cyclic quasi-static test was no longer

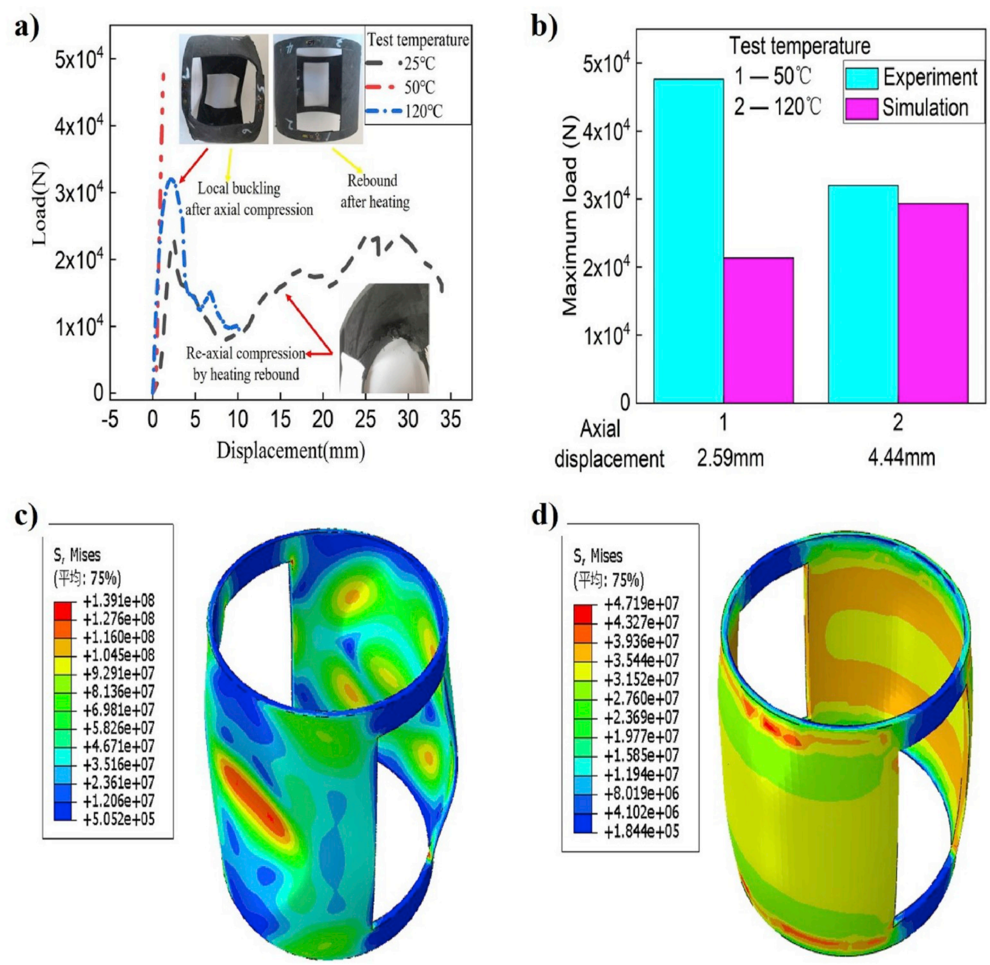

Fig. 12. Two rectangular holes (50 mm × 80 mm) are machined in the relative symmetrical position in the middle of the specimen tube: (a) The load-displacement curves of the specimen tube under axial compression loading at 50 °C and 120 °C, respectively, and at 25 °C after rebound are obtained. (b) Contrast diagram of maximum load achieved at the same displacement (experiment and simulation). (c) Stress distribution under maximum external loading at experimental temperature (50 °C). (d) Stress distribution under maximum external loading at experimental temperature (120 °C).

linear, the damage process began [25,26].

Taking the elliptical hole in Fig. 17 as an example, the mechanical model was established. The stress concentration was natural to occurred at the hole edge, which should be studied emphatically. According to the solution of complex variable function, the expression of stress at the edge of the elliptic hole has been obtained as follows:

$$\sigma_\theta = -q\frac{1-m^2-2m+2\cos 2\theta}{1+m^2-2m\cos 2\theta} \tag{7}$$

where $m = \frac{a-b}{a+b}$.

According to Eq (7), when $\theta = 0,\pi$, then $\sigma_{\max} = -q\left(\frac{2a}{b}+1\right)$, and, when $\theta = \pm\frac{\pi}{2}$, then $\sigma_{\min} = q$.

The external load is q, which indicates that the stress at $\theta = \pm\frac{\pi}{2}$ is the same as the external load. Take point A at the edge of the elliptical hole in Fig. 17 as a reference, transverse stress is as follows:

$$\sigma_2 = \sigma_\theta\cos\left(\theta-\frac{\pi}{4}\right) \tag{8-a}$$

When the transverse stress σ_2 reaches the strength of the matrix, the delamination of the matrix results in the failure of the structure. Taking the elliptical hole size of the specimen tube in Fig. 13 as an example, and assume that the external load $q = 1$, therefore, the expression of transverse stress is as follows:

$$\sigma_2 = \frac{25\cos 2\theta+7}{5\cos 2\theta-13} \tag{8-b}$$

When $\theta \in [0,2\pi]$, the functional image of transverse stress σ_2 and angle θ can be drawn as Fig. 18.

As seen from Fig. 18, when $\theta = 0,\pi$, the stress σ_2 is the largest, but the minimum σ_2 is 0. In addition, the yield strength and the equivalent modulus of the structure decreased exponentially with the increase of axial compression times. The failure modes of the matrix under tension and compression are described according to Hashin failure criteria [27].

When $\sigma_2 = -q\frac{1-m^2-2m+2\cos 2\theta}{1+m^2-2m\cos 2\theta}\cos\left(\theta-\frac{\pi}{4}\right) > \sigma(n,t)$, the matrix fails. When the temperature is constant, the stress can be regarded as a function on the number of compressions as follows:

$$\sigma(n) = kn^\alpha \tag{9}$$

Owing to $k > 0$ and $\alpha < 0$, the matrix will fail when $\sqrt[\alpha]{\frac{q(1-m^2-2m+2\cos 2\theta)}{k(1+m^2-2m\cos 2\theta)}\cos\left(\theta-\frac{\pi}{4}\right)} < n$. Assume that m and θ are fixed values, and that k and α are fixed values when specific materials and structures are used. $n = 1$, that is, when the first axial compression occurs, the external load q is the largest, but $\sqrt[\alpha]{\frac{q(1-m^2-2m+2\cos 2\theta)}{k(1+m^2-2m\cos 2\theta)}\cos\left(\theta-\frac{\pi}{4}\right)}$ is the smallest. With the increase of n (i.e. $n = 2,3,4\cdots$), the matrix will fail when $\sqrt[\alpha]{\frac{q(1-m^2-2m+2\cos 2\theta)}{k(1+m^2-2m\cos 2\theta)}\cos\left(\theta-\frac{\pi}{4}\right)} < n$.

When $a = b$, the elliptical hole becomes a circular hole, and $m = 0$, simultaneously, when $\sigma_2 = q(1+2\cos 2\theta)\cos\left(\theta-\frac{\pi}{4}\right) > \sigma(n)$, the matrix will fail. Assuming that the external load $q = 1$, then $\sigma_2 = (1+2\cos 2\theta)\cos\left(\theta-\frac{\pi}{4}\right)$, when $\theta \in [0,2\pi]$, the curve of the function (i.e., stress σ_2 and angle θ) is presented in Fig. 19.

As present in Fig. 19, in comparison to the elliptical hole, the maximum transverse stress of the circular hole was smaller than that of

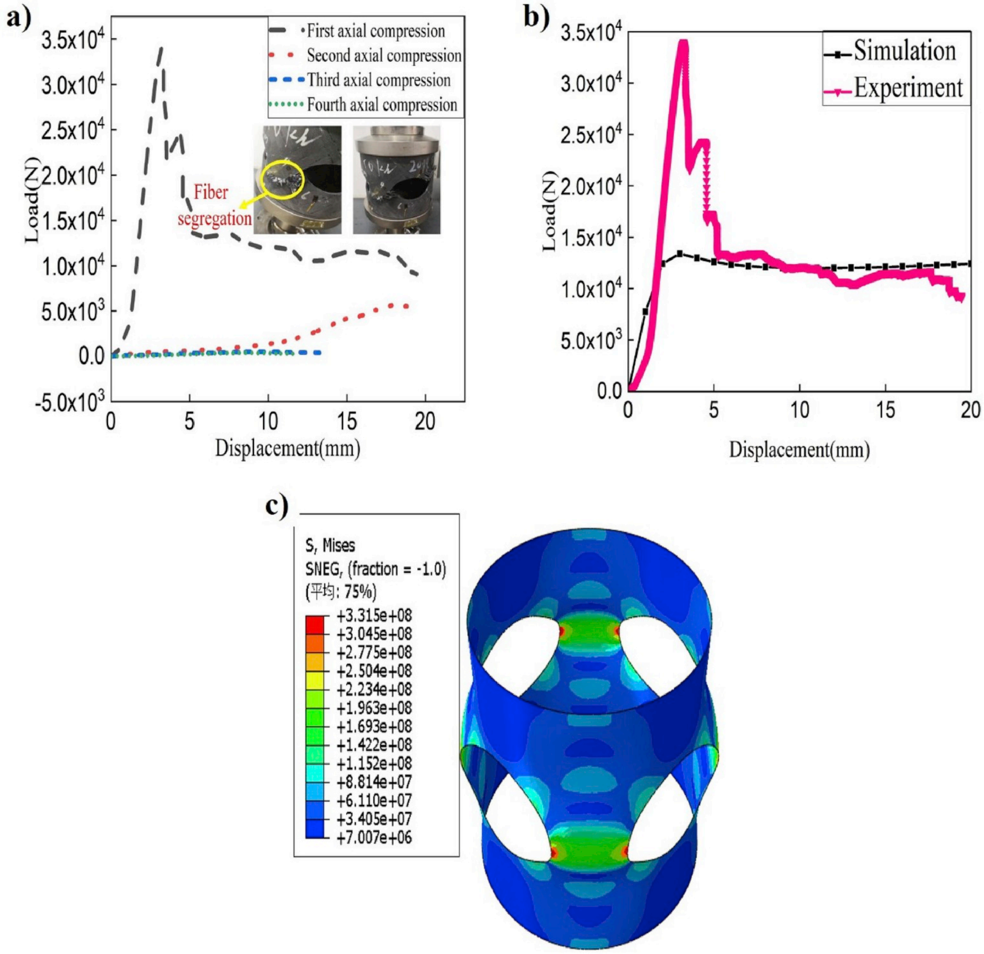

Fig. 13. Four elliptical defect holes distributed in the middle of the specimen tube (long axis: 60 mm, short axis: 40 mm): (a) Load-displacement curves under different axial compression times. (b) Load-displacement curves of experiment and simulation. (c) Stress contour of specimen tube under buckling load.

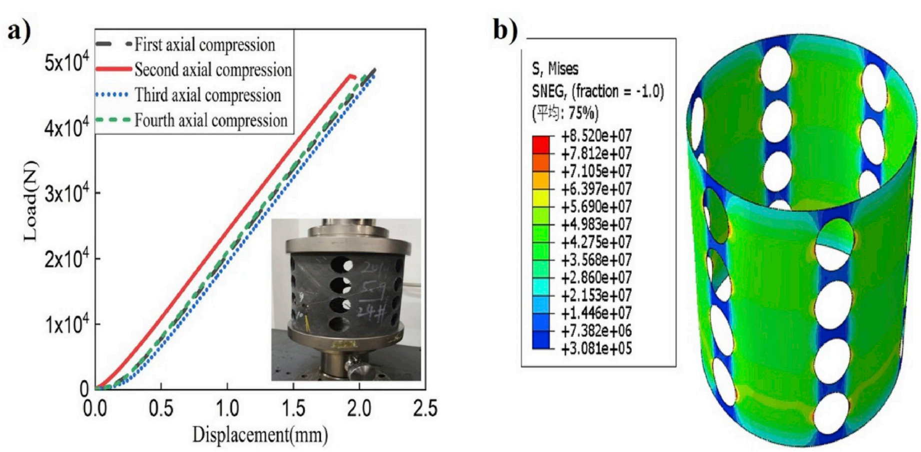

Fig. 14. (a) Load-displacement curves of specimen tube under different axial compression times. (b) Contour of stress distribution of specimen tube under maximum axial compression load.

the elliptical hole, indicating that the structural strength of the circular hole defect was higher than that of the elliptical hole defect.

In addition to elliptical and circular holes, there were corresponding stress expressions for rectangular holes. In comparison to elliptic holes, the stress distribution on the edge of rectangular holes was more complex, so the solution of complex variable function must be adopted. Based on Lei et al.'s research on stress distribution at the edge of rectangular holes via complex function method, the relationship between the number of axial compression and the strength of rectangular holes processed by shape memory material specimens was further analyzed, and Lei et al.'s research is as follows [28]:

Suppose a rectangular hole (where l and w = length and width of the hole, respectively), as shown in Fig. 20.

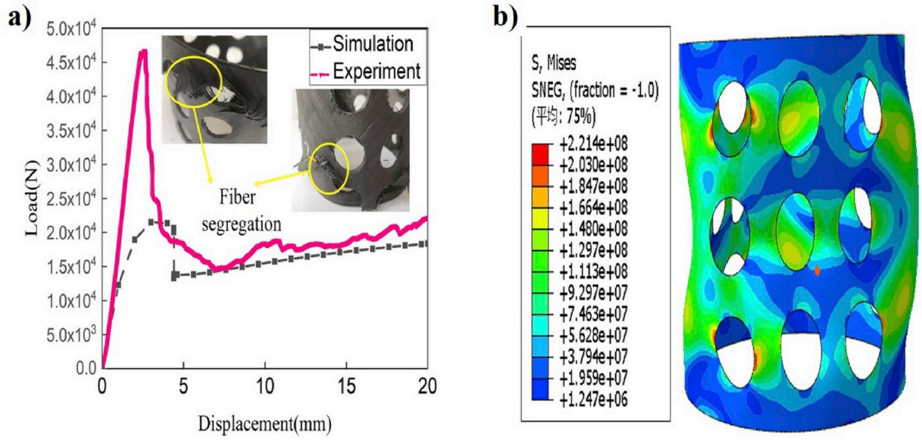

Fig. 15. (a) Load-displacement curves of experiment and simulation. (b) Stress contour of specimen tube under buckling load.

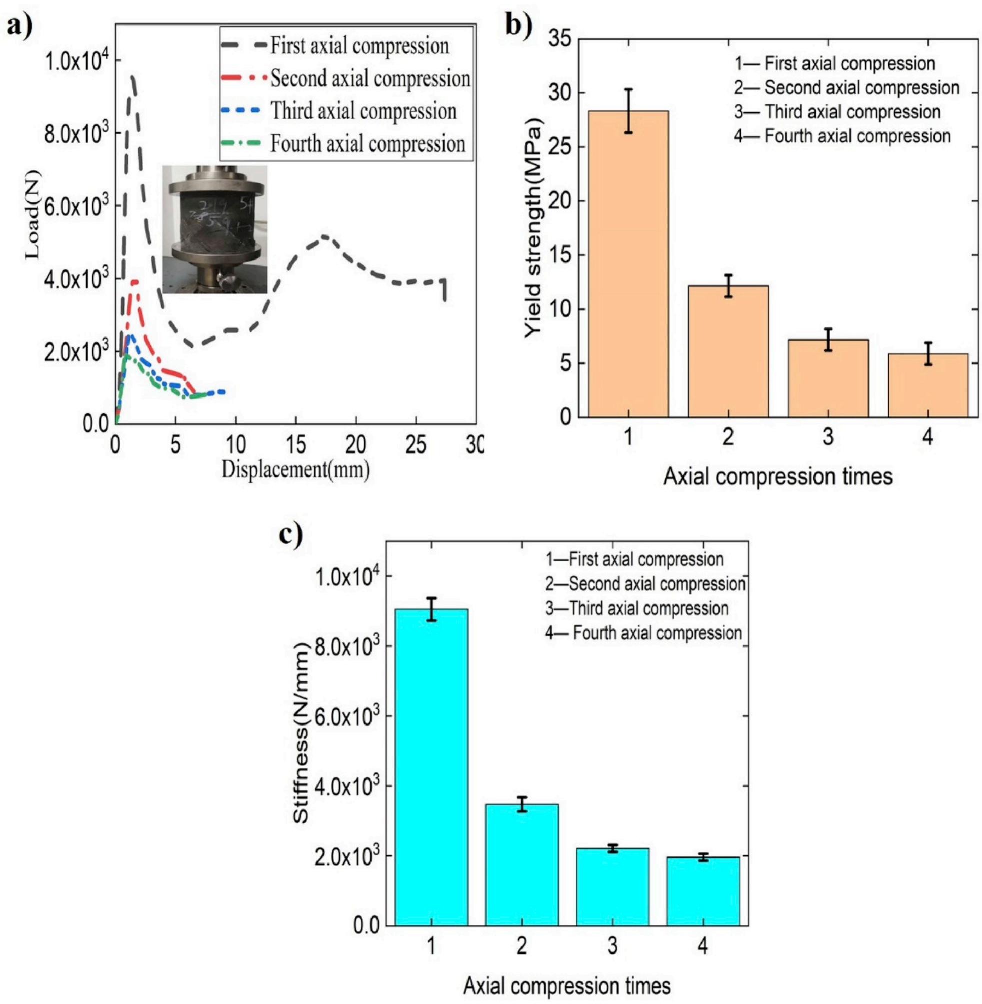

Fig. 16. (a) Load-displacement curves of specimen tube under different axial compression times. (b) Yield strength of specimen tube under different axial compression times. (c) Stiffness of specimen tube under different axial compression times.

$$\lambda_0 = {}^{l}\!/_{w} \quad \lambda = f\lambda_0 \tag{10a-b}$$

An equation for obtaining f can be derived as follows:

$$15\lambda_0^2 f^3 + \left(22\lambda_0 - 13\lambda_0^2\right)f^2 + (13 - 22\lambda_0)f - 15 = 0 \tag{11}$$

Adopting conformal transformation, the region occupied by elastomer in Z plane (i.e., X–Y plane) is transformed into that in ζ plane, and the following transformation equation is obtained:

$$Z = \omega(\zeta) = R\left(\frac{1}{\zeta} + A\zeta + B\zeta^3 + C\zeta^5\right) \tag{12}$$

Where

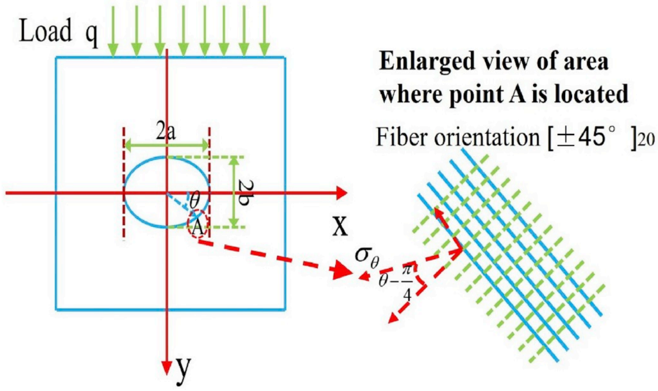

Fig. 17. Mechanical model of elliptical hole on the wall of specimen tube under axial compression.

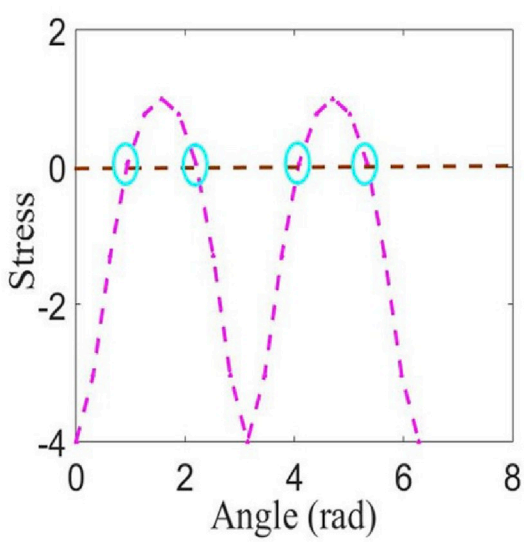

Fig. 18. Transverse stress-angle function curve of elliptic hole edge.

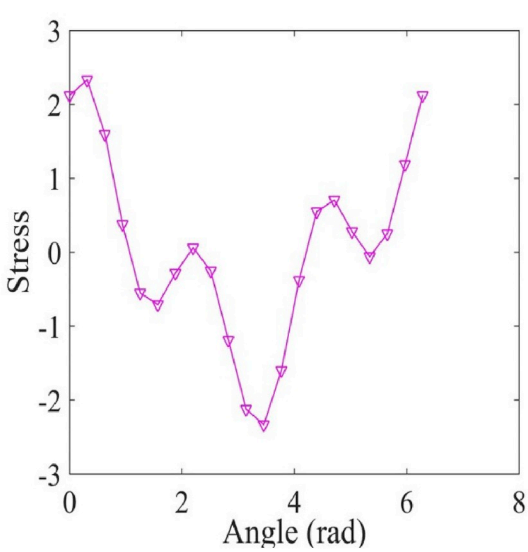

Fig. 19. Transverse stress-angle function curve of circular hole edge.

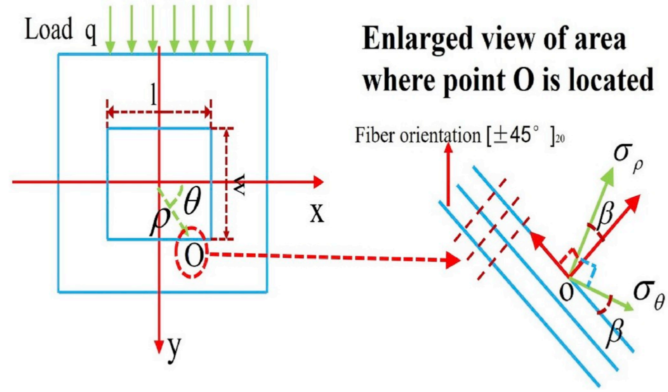

Fig. 20. Mechanical model of rectangular hole on the wall of specimen tube under axial compression loading.

$$A=\frac{\lambda-1}{\lambda+1};\ B=-\frac{2\lambda}{3(\lambda+1)^2};\ C=-\frac{2\lambda(\lambda-1)}{5(\lambda+1)^3} \tag{13a-c}$$

$$R=\frac{15(\lambda+1)^3}{4f(15\lambda^2+22\lambda+13)}w \tag{13d}$$

When $\rho = 1$, the hole problem is transformed into the unit circumference, which is the most common form. In ζ plane, $\zeta = \rho e^{i\theta}$, when $\rho = 1$, $\zeta = e^{i\theta} = \cos\theta + i\sin\theta$. Assuming only the plane stress state is considered, the following equations can be obtained:

$$\sigma_\theta+\sigma_\rho=q\left[-1+2\mathrm{Re}\frac{3t_6\zeta^4+t_7\zeta^2-1}{t_0}\right] \tag{14a}$$

$$(\sigma_\theta-\sigma_\rho+2i\tau_{\rho\theta})e^{-2i\delta}=2\left[\frac{\overline{\omega(\zeta)}}{\omega'(\zeta)}\Phi'(\zeta)+\psi(\zeta)\right] \tag{14b}$$

where Re represents the real part of a complex variable, and

$$e^{2i\delta}=\frac{\zeta^2}{\rho^2}\frac{\omega'(\zeta)}{\overline{\omega'(\zeta)}}=\frac{t_0}{t_9}\zeta^4\rho^2 \tag{14c}$$

$$\frac{\overline{\omega(\zeta)}}{\omega'(\zeta)}\Phi'(\zeta)=-qt_8\left\{\begin{array}{l}\left[\left(15C\zeta^4-3A\right)\left(t_6\zeta^4-1\right)\right.\\+t_7\zeta^4\left(10C\zeta^2+3B\right)\\\left.+6a_2\zeta^2+(a_1-3A)\right]/t_0^3\zeta^2\rho^2\end{array}\right\} \tag{14d}$$

$$\begin{aligned}\psi(\zeta)=&-\frac{q}{2}\frac{1}{t_0}\Big[-t_1+(a_0'a_1+t_2-3t_3a_2)\zeta^2\\&+6a_0a_2\zeta^3+(3a_0'a_2+15Ct_3)\zeta^4\\&-20Ca_0\zeta^5-5Ca_0'\zeta^6\Big]\end{aligned} \tag{14e}$$

$$a_0'=-\frac{5Ct_3t_{10}\zeta^4+(t_2+3Bt_3)t_{11}\zeta^2+(t_4+At_3)t_{12}}{t_0^2} \tag{14f}$$

$$a_1=\frac{\cos 2\alpha-t_4}{t_5-t_3}+\frac{\sin 2\alpha}{t_5+t_3}i \qquad a_2=\frac{\mathrm{C}\cos 2\alpha-(1-B)t_3}{t_5-t_3}-\frac{\mathrm{C}\sin 2\alpha}{t_5+t_3}i \tag{14g-h}$$

$$a_0=\zeta\frac{5Ct_3\zeta^4+(t_2+3Bt_3)\zeta^2+(t_4+At_3)}{t_0} \tag{14i}$$

When $\alpha = -\frac{\pi}{2}$, the external load acts on the specimen tube as axial compression loading.

$$t_0=5C\zeta^6+3B\zeta^4+A\zeta^2-1;\ \ t_1=e^{-2i\alpha};\ \ t_2=1+5C^2 \tag{14j-l}$$

$$t_3 = B + AC; \quad t_4 = A + 3BC \quad t_5 = 1 - 3C^2 \tag{14m-o}$$

$$t_6 = B + a_2; \quad t_7 = A + a_1; \quad t_8 = \zeta^6 + A\rho^4\zeta^4 + B\rho^8\zeta^2 + C\rho^{12} \tag{14p-r}$$

$$t_9 = A\rho^4\zeta^4 + 3B\rho^8\zeta^2 + 5C\rho^{12} - \zeta^6 t_{12} = 25C\zeta^6 + 9B\zeta^4 + A\zeta^2 + 1; \quad t_{10} = 5C\zeta^6 - 3B\zeta^4 - 3A\zeta^2 + 5 \tag{14s-t}$$

$$t_{11} = 15C\zeta^6 + 3B\zeta^4 - A\zeta^2 + 3; \quad t_{12} = 25C\zeta^6 + 9B\zeta^4 + A\zeta^2 + 1 \tag{14u-v}$$

Based on the above formulas, the stress distribution (σ_θ, σ_ρ and $\tau_{\rho\theta}$) on the edge of a rectangular hole can be obtained. With regard to elliptical holes, matrix failure is the main factor in the process of axial compression loading. As shown in Fig. 20, taking a random point O at the edge of the rectangular hole as the reference point, the transverse stress in the vertical direction of the fibers is as follows:

$$\sigma_2 = \sigma_\rho \cos\beta + \sigma_\theta \sin\beta \tag{15}$$

When $\sigma_2 > \sigma(n) = kn^\alpha$, delamination failure phenomenon of the matrix will occur, where β varies with the position of the action point on the edge of a rectangular hole, in addition, σ_θ and σ_ρ can be obtained from the stress complex function equations (14a) and (14b). In pace with the number of axial compression increase, $\sigma(n)$ decreases gradually, therefore, the transverse stress σ_2 decreases gradually when the structure is delaminated.

In Figs. 17 and 20, elliptical and rectangular defect holes were machined on the tube wall respectively, and stress concentration around the defect holes was analyzed under the action of axial compression loading. Combining with the unique shape memory effect of SMPCs, Hashin failure criteria and the previous methods were used, simultaneously, the failure model of CFRP-wound tube under axial compression loading was modified by complex function method. Based on the above two modified mechanical models, the stress distribution in the defect area of shape memory polymer composite tube under axial compression loading could be well explained.

4. Conclusion

In this paper, the mechanical response of composite tubes with shape memory resin as matrix, carbon fiber winding with (±45°) under radial and axial compression loading was investigated. Simultaneously, the change of strength, modulus of the whole structure of the specimen tubes after processing defective holes with different shape and size on the tube wall was analyzed. When the specimen tube was compressed radially, the cross-section of the specimen tube changed from circular to elliptical. During the deformation process, debonding occurred between the fiber layers, in addition, the separation between the fiber layers became larger gradually, and the fibers are finally peeled off from the matrix. Afterwards, the specimen tube after radial compression loading, was recovered to the original shape after external excitation, and then the radial compression was carried out again, and the radial strength decreased with the increase on the number of radial compression, indicating that the shape of the specimen tube has been recovered, but the strength not, that is, the bonding state between the fiber layers was unable to be recovered. The radial compressive experiment of the specimen tube showed that the buckling load and the axial equivalent modulus of the specimen tube decreased with the increase of the experimental temperature. The larger the defect hole was, the lower the buckling load and equivalent modulus of the specimen tube would be. Besides, under the condition of the same defect hole area, the buckling load of the specimen tube with dispersed defect hole was higher than that of the specimen tube with concentrated defect, and the strength of the specimen tube with sharp defect hole was lower than that with non-sharp defect hole. As present in the axial compressive testing, we could find that the location of local buckling is basically in the middle of the specimen, and the material delamination phenomenon occurred, indicating that the axial compression was mainly the load-bearing effect of the matrix, not the fiber. As a result of the shape memory effect of the material used, the specimen tube could be recovered to initial shape after external excitation, furthermore, the buckling load and the axial equivalent modulus of the specimen tube decreased in the form of power function after repeated compression. Based on the previous research and combined with the shape memory effect of the specimen tube, a mechanical model for delamination failure model of defect holes under axial compression loading was established.

Declaration of competing interest

We would like to declare on behalf of all authors that the work described is original research that has not been published previously and is not under consideration for publication elsewhere. The publication of the manuscript entitled "Damage and failure in carbon fiber-reinforced epoxy filament-wound shape memory polymer composite tubes under compression loading", is approved by all authors and tacitly or explicitly by the responsible authorities where the work was carried out. If accepted, it will not be published elsewhere in the same form, in English or in any other language, without the written consent of Polymer testing.

Acknowledgements

This work is supported by the National Natural Science Foundation of China (Grant Nos.11632005 and 11672086).

References

[1] R. Rafiee, On the mechanical performance of glass-fibre-reinforced thermosetting-resin pipes: a review, Compos. Struct. 143 (2016) 151–164.
[2] G. Perillo, R. Vacher, F. Grytten, S. Sørbø, V. Delhaye, Material characterisation and failure envelope evaluation of filament wound GFRP and CFRP composite tubes, Polym. Test. 40 (2014) 54–62.
[3] R. Rafiee, M.A. Torabi, S. Maleki, Investigating structural failure of a filament-wound composite tube subjected to internal pressure: experimental and theoretical evaluation, Polym. Test. 67 (2018) 322–330.
[4] J.H.S. Almeida, M.L. Ribeiro, V. Tita, S.C. Amico, Damage modeling for carbon fiber/epoxy filament wound composite tubes under radial compression, Compos. Struct. 160 (2017) 204–210.
[5] J. Xing, P. Geng, T. Yang, Stress and deformation of multiple winding angle hybrid filament-wound thick cylinder under axial loading and internal and external pressure, Compos. Struct. 131 (2015) 868–877.
[6] Y.C. Jung, H.H. So, J.W. Cho, Water-responsive shape memory polyurethane block copolymer modified with polyhedral oligomeric silsesquioxane, J. Macromol. Sci. Part B Physics 45 (2006) 453–461.
[7] P.R. Buckley, G.H. McKinley, T.S. Wilson, W. Small, W.J. Benett, J.P. Bearinger, M. W. McElfresh, D.J. Maitland, Inductively heated shape memory polymer for the magnetic actuation of medical devices, IEEE (Inst. Electr. Electron. Eng.) Trans. Biomed. Eng. 53 (2006) 2075–2083.
[8] A.M. Schmidt, Electromagnetic activation of shape memory polymer networks containing magnetic nanoparticles, Macromol. Rapid Commun. 27 (2006) 1168–1172.
[9] A. Lendlein, H.Y. Jiang, O. Junger, R. Langer, Light-induced shape memory polymers, Nature 434 (2005) 879–882.
[10] T.F. Scott, A.D. Schneider, W.D. Cook, C.N. Bowman, Photoinduced plasticity in cross-linked polymers, Science 308 (2005) 1615–1617.
[11] Zbigniew Kolakowski, Tomasz Kubiak, Interactive dynamic buckling of orthotropic thin walled channels subjected toin plane pulse loading, Compos. Struct. 81 (2007) 222–232.
[12] Jiarang Fan, Jianqiao Ye, An exact solution for the static and dynamics of Laminated thick plates with orthotropic layers, Int. J. Solid Struct. 26 (1990) 655–662.
[13] Jiarang Fan, Jianqiao Ye, Exact solution of buckling for simply support thick laminates, Compos. Struct. 24 (1993) 23–28.
[14] C.C. Lin, S.H. Cheng, J.T.S. Wang, Local buckling of delaminated of composite sandwich plates, J. AIAA 34 (1996) 2176–2183.
[15] S.H. Cheng, C.C. Lin, J.T.S. Wang, Local buckling of delaminated sandwich beams using continues analysis, Int. J. Solid Struct. 34 (1997) 275–288.
[16] H. Chai, C.D. Babcock, W.G. Knayss, One dimensional modeling of failure laminated plates by delamination buckling, Solids Struct. 17 (1981) 1069–1083.
[17] A.J. Vizzini, P.A. Lagace, The buckling of a delaminating sublaminate on an elastic foundation, Compos. Mater. 21 (1987) 1106–1117.
[18] P.M. Weaver, J.R. Driesen, P. Roberts, Anisotropic effects in the compression buckling of laminated composite cylindrical shell, Compos. Sci. Technol. 62 (2002) 91–105.

[19] Tafreshi Azam, Buckling and post-buckling analysis of composite cylindrical shell with cutouts subject to internal pressure and axial compression loads, Int. J. Pres. Ves. Pip. 79 (2002) 351–359.
[20] Marco Cerini, Brian G. Falzon, Use of Arc-Length method for capturing mode jumping in postbuckling aerostructures, AIAA J. 43 (2005) 239–246.
[21] S.A.M. Ghannadpour, A. Najafi, B. Mohammadi, On the Buckling Behavior of Cross-Polylaminate Composite Plates Due to Circular/elliptical Cutouts, Aerospace Engineering Department, Amirkabir University of Technology, Tehran, Iran, 2006, pp. 156–165. Available online 16 June.
[22] Xinsheng Xu, Jianqing Ma, C.W. Limb, Hongjie Chu, Dynamic local and global buckling of cylindrical shells under axial impact, Eng. Struct. 31 (2009) 111–140.
[23] M.L. Ribeiro, V. Tita, D. Vandepitte, A new damage model for composite laminates, Compos. Struct. 94 (2012) 635–642.
[24] A. Puck, H. Schürmann, Failure analysis of FRP laminates by means of physically based phenomenological models, Compos. Sci. Technol. 58 (1998) 1045–1067.
[25] P. Ladeveze, E. LeDantec, Damage modelling of the elementary ply for laminated composites, Compos. Sci. Technol. 43 (1992) 257–267.
[26] A. Matzenmiller, J. Lubliner, R.L. Taylor, A constitutive model for anisotropic damage in fiber-composites, Mech. Mater. 20 (1995) 125–152.
[27] Z. Hashin, Failure criteria for unidirectional fiber composites, J. Appl. Mech. 47 (1980) 329–334.
[28] G.H. Lei, Stress and displacement around an elastic artificial rectangular hole, J. Eng. Mech. 129 (2001) 880–890.